Effect of the stress state on ultimate strain energy density in the failure of reinforced epoxy resin

D. I. Vichuzhanin, S. V. Smirnov
Institute of Engineering Science, Ural Branch of the Russian Academy of Sciences, Russia
mmm@imach.uran.ru, http://orcid.org/0000-0002-6508-6859
smirnov.sergy@hk.ru, http://orcid.org/0000-0002-2083-5377

A. V. Pestov, V. A. Osipova
Postovskii Institute of Organic Synthesis, Ural Branch of the Russian Academy of Sciences, Russia
pestov@ios.uran.ru, http://orcid.org/0000-0002-4270-3041
osipova.sva@gmail.com, http://orcid.org/0000-0001-7451-9428

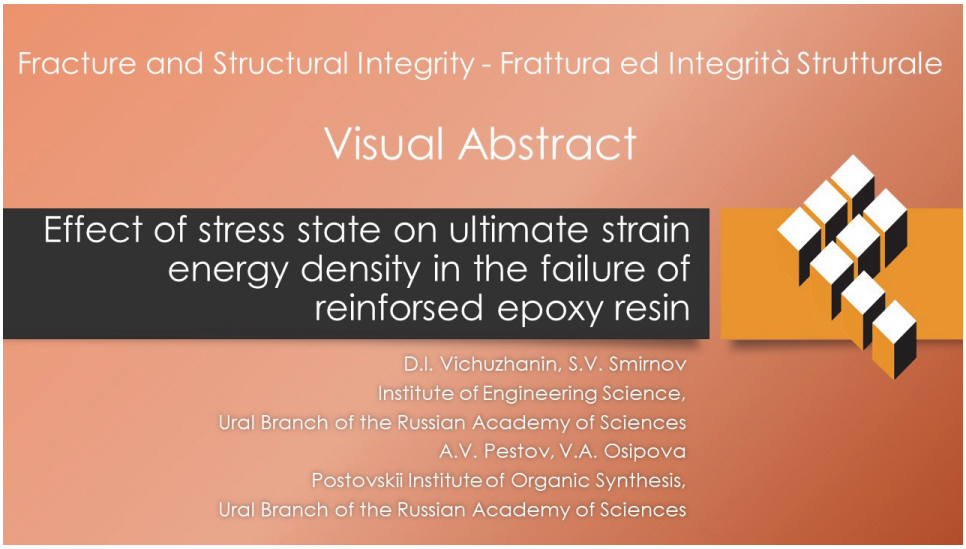

Citation: Vichuzhanin, D.I., Smirnov, S.V., Pestov, A.V., Osipova, V.A., Effect of the Stress State on Ultimate Strain Energy Density in the Failure of Reinforced Epoxy Resin, Fracture and Structural Integrity, 75 (2026) 220-237.

Received: 30.07.2025
Accepted: 16.10.2025
Published: 01.11.2025
Issue: 01.2026

KEYWORDS. Epoxy Resin, Stress triaxiality factor, Lode–Nadai coefficient, Strain energy density.

INTRODUCTION

Epoxy materials are used in construction, mechanical engineering, and household appliances as protective coatings, sealers, glues, impregnating and repair materials. In the processes, the structural components may experience a complex stress-strain state under conditions of both low and high temperatures. In view of the trend for an ever-increasing use of these materials in state-of-the-art structures and mechanisms, it is relevant to predict their failure under service loads. The stress state in compressive, tensile, bending, and other tests regulated by standards is generally different

from that under service conditions. Therefore, the results of these tests can be used only for qualitative or comparative estimation of material serviceability. The effect of the stress state on the failure of adhesives is being actively studied in terms of fracture mechanics, which studies conditions for the evolution of existing cracks appearing on the interfaces of adhesive joints or in laminated metal-polymer materials (see recent reviews [1-2]).

Significant experience in the quantitative description of limiting states under conditions of different stress states has been gained in studying the failure of metal materials. In order to predict the risk of failure under planned loading conditions, the fracture criteria depending on the invariant characteristics of the stress state are generally used. Experimental procedures in which, by varying the shape of specimens made of materials under study (mainly metal ones), one can change the stress state and use the experiment results to identify the fracture criteria or damage models are described in the literature [3–5].

As a rule, the stress triaxiality factor k and the Lode–Nadai coefficient μ_σ (or the Lode normed angle $\bar{\theta}$) are currently being used in fracture testing to characterize the stress state [4–9], which are calculated by the formulas:

$$k = \frac{\sigma}{T}; \tag{1}$$

$$\mu_\sigma = \frac{2\sigma_{22} - \sigma_{11} - \sigma_{33}}{\sigma_{11} - \sigma_{33}}; \ \bar{\theta} = 1 - \frac{2}{\pi}\arccos\left(\frac{3\sqrt{3}J_3}{2J_2^{3/2}}\right), \tag{2}$$

where $\sigma = \frac{\sigma_{11} + \sigma_{22} + \sigma_{33}}{3}$ is the mean normal (hydrostatic) stress; $T = \frac{1}{\sqrt{6}}\sqrt{(\sigma_{11} - \sigma_{22})^2 + (\sigma_{22} - \sigma_{33})^2 + (\sigma_{33} - \sigma_{11})^2}$ is tangential stress intensity; σ_{11}, σ_{22} and σ_{33} are principal stresses; J_2 and J_3 are the second and third invariants of the stress deviator. Normal tensile stresses prevail when $k > 0$, compressive ones being dominant when $k < 0$. The Lode–Nadai coefficient characterizes the form of the stress state. The values $\mu_\sigma = \pm 1$ correspond to the axisymmetric compression/tension state, and there is a plane strain state when $\mu_\sigma = 0$. The values $\bar{\theta} = \pm 1$ correspond to the axisymmetric tension/compression state, whereas $\bar{\theta} = 0$ corresponds to the plane strain state.

The effect of the parameters defined in Eqs. (1) and (2) on ultimate fracture characteristics are studied in detail for metal materials ([5–9] etc.), but these dependences for polymers and adhesives have yet to be studied. There are separate data on the effect of the stress triaxiality factor k in the region of tensile stresses, which were obtained in tensile and bending testing of specimens with stress concentrators [10-11], in tension and compression [12]. Complex testing of epoxy resin by various methods were discussed in [13]. In [14] thin-walled tubular specimens made of hardened epoxy resin were subjected to torsion combined with axial loading, external and internal pressure. The features of the experimental procedures made it impossible to reach high hydrostatic pressure ($p < 17.24$ MPa at a yield stress of ≈ 60 MPa). This may be why the authors concluded that hydrostatic pressure had no effect on ultimate strain properties, although this effect was significantly manifested when the tensile and compressive test results were compared.

Testing in high-pressure chambers was formerly widely used to construct fracture loci of metal materials. The test results enabled the influence of the parameters defined by Eqs. (1) and (2) on ultimate strain properties [15-16, etc.] to be correctly separated; however, due to the complexity of conducting such experiments, the majority of studies now use testing of differently shaped specimens. Besides, this was favored by the development of numerical methods for stress-strain analysis, which make it possible to calculate the values of the stress state parameters in testing.

Besides widespread testing for uniaxial tension, compression, and torsion, where $k = \frac{1}{\sqrt{3}}$, $-\frac{1}{\sqrt{3}}$ and 0, $\mu_\sigma = -1$, $+1$ and 0, respectively, irregularly shaped specimens are used to extend the range of variation of the stress state. Thus, e.g., butterfly-shaped specimens are used for testing at $\mu_\sigma = 0$ [17–18].

These specimens allow k to be varied in a fairly wide range, between −0.33 and 1.73. However, to test these specimens, it is necessary to use a testing machine with two independent perpendicularly positioned drives. For testing under conditions of the conservative value $\mu_\sigma = 1$ Nakajima specimens are used [19], the value $k = 1.09$ being also constant. The fracture locus is plotted from the test results, showing the amount of strain accumulated before fracture ε_f as a function of the stress coefficients.

In our earlier papers we proposed a set of tests enabling us to study the deformability of metal materials in the range of variation of the stress parameters $-1 \le \mu_\sigma \le 1$ and $-0.6 \le k \le 1.2$ [7]. Besides standard tensile and compressive testing of cylindrical specimens, the set includes tensile and compressive testing of bell-shaped specimens and dishing of thick-walled cup-shaped specimens. The set of tests was tried out on studying a number of aluminum alloys and metal matrix composites [7, 20–22], and even at high temperatures. It is of interest to extend the proposed approach to studying the effect of the stress state on the characteristics of the cohesive failure of organic polymer materials. Epoxy materials are known for their low plastic properties; therefore, it is difficult to use strain ε_f as a limiting characteristic to plot a fracture locus for them since its values are small. Therefore, in this paper, the notion of *fracture locus* includes *strain energy density* instead of *strain* or *amount of strain.*

The intention of this study is to modify and adapt the set of tests [7] for studying the effect of the stress parameters and temperature on the cohesive failure of epoxy resin in order to represent the research results in the form of a fracture locus.

RESEARCH MATERIAL

Promising TiO_2-reinforced epoxy resin is used as the research material. The ED-20–4,4'-isopropylidenediphenol commercial epoxy-diane resin with the epoxy number 21.1% was made at Sverdlov Plant, Dzerzhinsk, Russia. Titanium oxide (TiO_2) nanoparticles (99.5% purity, an average size 21 nm) were made by Sigma-Aldrich (Germany). The epoxy resin was preliminarily dissolved in tetrahydrofuran, 10 wt% of TiO_2 was added to the resulting solution, and this was processed in a ball mill for 4 hours. Polyethylenepolyamine was added in a 10:1 ratio for curing, and, after mixing, this was poured into split Teflon molds, and this excludes the appearance of mechanical stress concentrators on the specimens. The reinforcement technology applied enabled us to obtain a uniform distribution of TiO_2, predominantly forming agglomerates with an average size of 1.2 μm, as is shown in fig. 1. Complete curing occurred in 24 hours at 25 °C. The curing conditions were set according to the recommendations of the resin producer, and no other conditions were studied. The effect of TiO_2 on the degrees of cure and the mechanical properties were studied earlier and discussed in [23]. Besides reinforced epoxy resin specimens, similar pure epoxy resin ones were made in order to detect the effect of adding the reinforcing agent on the deformability of the epoxy resin at the same time.

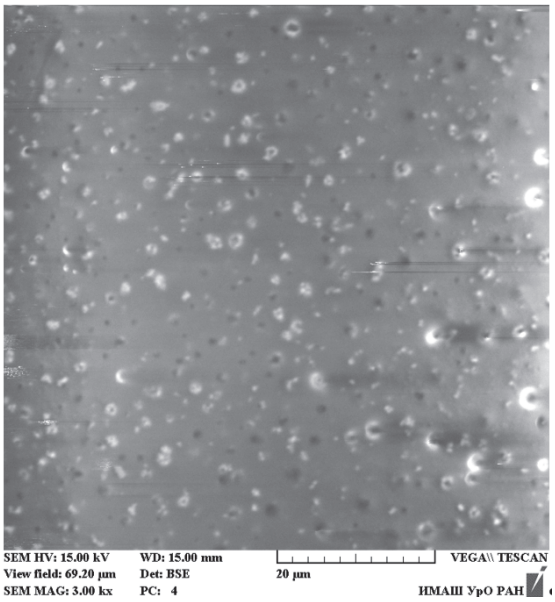

Figure 1: TiO_2 nanoparticle agglomerate distribution.

Bell-shaped tensile and compressive specimens and thick-walled cup-shaped specimens to be tested under axisymmetric deformation were made by analogy with those described in [7], though their geometric dimensions were appropriately adjusted (fig. 2 a, b, c). The specimens (fig. 2 d) reported in [23] were used for shear testing under plane strain. The cylindrical compressive specimens had a diameter of 4 mm and a height of 6 mm.

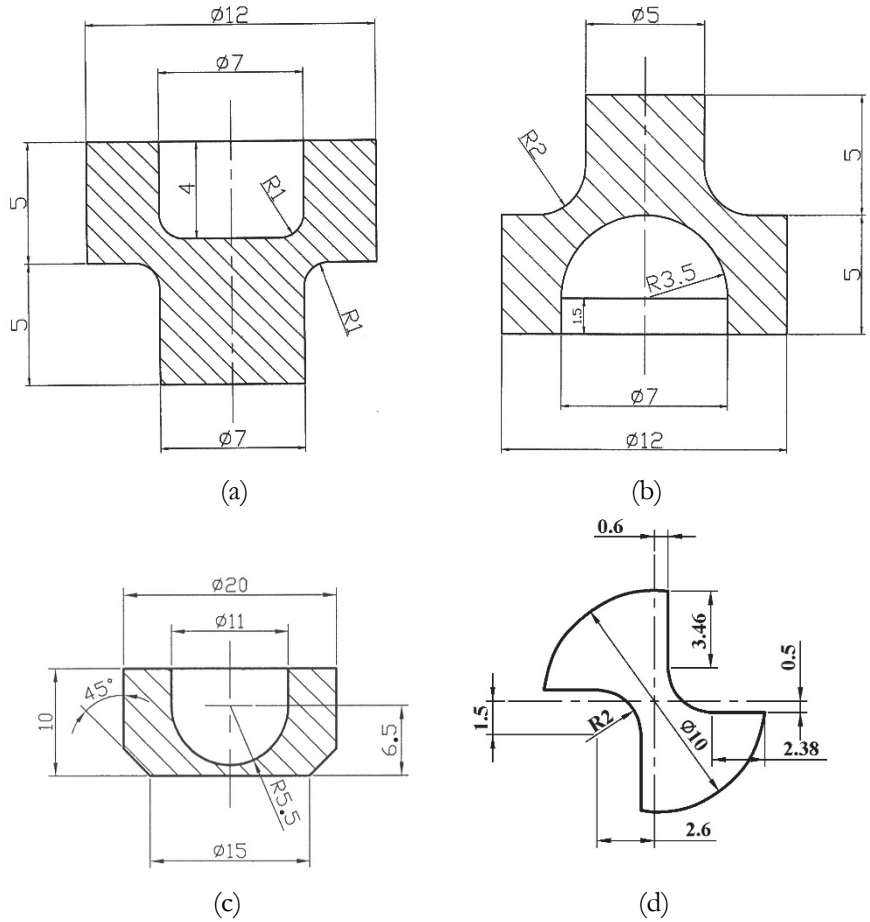

Figure 2: Outlines of the specimens: bell-shaped tensile specimen (a); bell-shaped compressive specimen (b); thick-walled cup-shaped specimen (c); oblique dog-bone-shaped specimen for shear testing under plane strain (d).

TEST EQUIPMENT

The specimens were deformed to fracture in an Instron 8801 servohydraulic testing machine at an actuator velocity of 1 mm/min. The machine has the following characteristics: a maximum loading force of 100 kN; a load measurement accuracy of 0.25% from the measured value; a displacement gauging accuracy of 0.1% from the measured value. The tests were performed in a temperature chamber enabling us to test the specimens at temperatures ranging from −70 to +300 °C. The Solidol-Zh grease was used to decrease friction between the deforming tool and the specimen.

The normal elastic modulus, the stress-strain curve, and the glass transition temperature were determined by means of a DMA Eplexor 100N test system for dynamic mechanical analysis, which determines the mechanical and thermomechanical material properties in the range of static loads from 0 to 1500 N and oscillating loads between 0 and 100 N at frequencies ranging between 0.1 and 100 Hz. The device is equipped with a climate chamber for testing at temperatures from −160 to +500 °C. The experiment results were recorded and processed by means of the EPLEXOR®9 specialized software.

To make certain that the specimen geometry allows us to achieve the required stress state during loading, we first constructed finite-element models of the specimens and simulated loading.

In order to achieve a satisfactory reproducibility of the tests, a lot of three specimens was used in each type of testing and the obtained results were averaged. Since the plastic strains before failure are insignificant, the reproducibility of the experiments was assessed from the value of the displacement U of the loading tool at the moment of failure, not from the geometric parameters of the failed specimens. A statistical analysis of the sample of the obtained values was made. The following was determined within the statistical analysis:

- the sample average value: $\bar{U} = \frac{1}{n}\sum_{i=1}^{n} U_i$, where n – is sample size;

- standard deviation: $S = \sqrt{\frac{1}{n-1}\sum_{i=1}^{n}\left(U_i - \bar{U}\right)^2}$;

- coefficient of variation: $CV = \frac{S}{\bar{U}} \cdot 100\%$.

The coefficient of variation for each specimen lot did not exceed 4.33%.

The relative deviation from the mean in terms of the value of ultimate strain before failure calculated by finite element simulation did not exceed ±8.5%.

THE RESULTS OF TESTING AND SIMULATING THE STRESS-STRAIN STATE

Compression of cylindrical specimens

The glass transition temperature $T_g = 78$ °C (TiO_2-reinforced epoxy resin) and 74 °C (pure epoxy resin) was determined by dynamic mechanical analysis according to ASTM D7028 by the test temperature dependence of the storage module at a static load of 20 N and an oscillating measuring load of 1.2 N with a frequency of 1 Hz. Therefore, at testing temperatures of −50 and 25 °C, the epoxy materials were vitrified.

To determine the stress-strain curves, cylindrical specimens were compressed by means of a DMA Eplexor 100N device using the Universal Test option, which provided testing under conditions of simple quasi-static loading. The use of this equipment was caused by the impossibility of using Instron 8801 to deform such small specimens.

Strain ε and flow stress σ_S were calculated by the formulas:

$$\varepsilon = \ln\left(\frac{h_0}{h}\right),\ \sigma_S = \frac{P}{F} \tag{3}$$

where h_0 and h are the initial and current specimen heights; P is the current compressive force; F is the current specimen cross-sectional area determined from the volume constancy condition by the formula:

$$F = \frac{F_0 h_0}{h} \tag{4}$$

The stress-strain curves obtained from the tests of specimens made of each material performed at −50 and 25 °C, which are limited by maximum stress corresponding to ultimate strength, are shown in fig. 3. The specimens were loaded at rates ranging between 1 and 10 s^{-1}. The analysis of the results has shown that the change of strain rate by an order of magnitude causes a 3% change in strain resistance at a test temperature of −50 °C and an 8% change at 25 °C, and this is below the 10% allowable natural variation of the strength properties for structural materials [24]. Therefore, averaged stress-strain curves were used in the simulation, without regard for the effect of strain rate. The average values of the normal elastic moduli E (Tab. 1) were determined on the linear lengths of the stress-strain curves of the specimens in the selected stress range of 20 to 60 MPa. The stress-strain curves were approximated by Eqn. (5) on the portion of linear elasticity and by the polynomial dependence represented by Eqn. (6) on the nonlinear one in the Statistica 8.0 software:

$$\sigma_{eq} = E\varepsilon_{eq}\ ,\ \left(\varepsilon_{eq} \le 0.015\right) \tag{5}$$

$$\sigma_{eq} = a_3\hat{\varepsilon}_{eq}^3 + a_2\hat{\varepsilon}_{eq}^2 + a_1\hat{\varepsilon}_{eq} + a_0\,,\ \hat{\varepsilon}_{eq} = 100\varepsilon_{eq}\,,\ \left(\varepsilon_{eq} > 0.015\right) \tag{6}$$

where ε_{eq} and σ_{eq} are equivalent stress and equivalent strain; a_3, a_2, a_1 and a_0 are approximation coefficients, whose values are shown in Tab. 1.

$$\varepsilon_{eq} = \frac{\sqrt{2}}{3}\sqrt{\left(\varepsilon_{11} - \varepsilon_{22}\right)^2 + \left(\varepsilon_{22} - \varepsilon_{33}\right)^2 + \left(\varepsilon_{33} - \varepsilon_{11}\right)^2} \tag{7}$$

$$\sigma_{eq} = \frac{1}{\sqrt{2}}\sqrt{(\sigma_{11}-\sigma_{22})^2 + (\sigma_{22}-\sigma_{33})^2 + (\sigma_{33}-\sigma_{11})^2} \quad (8)$$

where ε_{11}, ε_{22} and ε_{33} are total principal strains, σ_{11}, σ_{22} and σ_{33} are total principal stresses.

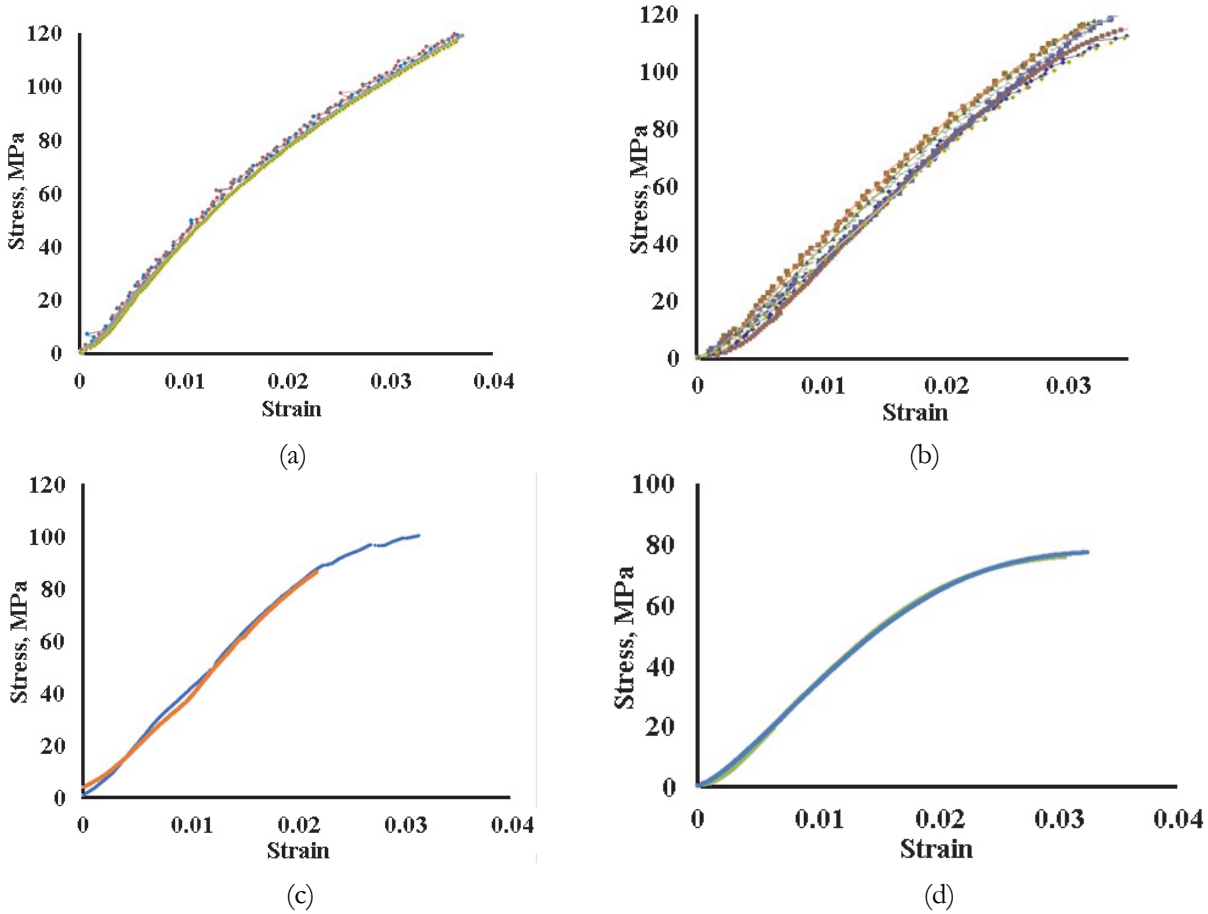

Figure 3: The stress-strain curves of reinforced epoxy resin (a, b) and pure epoxy resin at −50 °C (a, c) and 25 °C (b, d).

	Reinforced epoxy resin					Pure epoxy resin				
T, °C	E, MPa	a_3, MPa	a_2, MPa	a_1, MPa	a_0, MPa	E, MPa	a_3, MPa	a_2, MPa	a_1, MPa	a_0, MPa
-50	4780	-2.216	10.82	28.06	6.41	4100	1.157	-20.91	100.03	-44.11
25	4170	-0.436	-3.08	54.25	-10.46	3770	1.708	-21.28	86.08	-36.28

Table 1: The values of the normal elastic modulus E and the coefficients of approximation of the stress-strain curves by Eqn. (6).

It follows from Tab. 1 and fig. 3 that the introduction of 10% of TiO_2 nanoparticles enhances the strength properties of epoxy resin; namely, the value of the normal elastic modulus increases by 14 and 11% at $T = -50$ and 25 °C, respectively, and the value of ultimate compressive strength increases by 25 and 35% at $T = -50$ and 25 °C, respectively.

In order to evaluate the characteristics of the stress-strain state, mathematical simulation was made by the finite element method. The Ansys finite element software was used for the simulation. The material of the deforming tool was treated as a perfectly rigid body, and the epoxy materials were considered to be isotropic elastoplastic materials with the deformation behavior described by Eqs. (5) and (6). The associated flow rule and the von Mises yield criterion were applied in the plastic region, the stress-strain curves were specified in the tabular form of the MISO model by using the results of calculations by Eqn. (6). The boundary conditions were set in displacements (U). Friction between the deforming tool and the specimen was described by the Amontons–Coulomb friction law with the friction coefficient $\mu = 0.1$. In view of the obvious axial symmetry of deformation, a half of the specimen cross-section was simulated. PLANE183 finite elements were used to

construct a grid model. Besides, a grid convergence study was conducted in order to avoid the effect of finite element sizes on the simulation results. The element sizes were varied between 1 and 0.1 mm. The solution results were compared by equivalent strain in the most probable specimen fracture zone (in the middle of the lateral surface). Fig. 4 exemplifies the dependence of equivalent strain on the sizes of the finite elements of the model. Staring from element sizes of 0.25 and smaller, the solution results differ by less than 1%. Finally, the number of finite elements in the model was 192, with an element size of 0.25 mm.

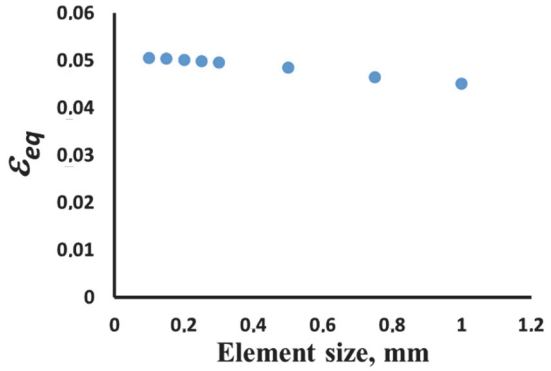

Figure 4: The results of the grid convergence study for the model of compressing a cylindrical pure epoxy resin specimen at a test temperature of 25 °C.

The adequacy of the constructed finite element models was also verified by comparing the experimentally obtained deformation forces with those calculated in the simulation. Fig. 5 exemplifies this comparison for compressive testing of cylindrical specimens of reinforced epoxy resin at 25 °C.

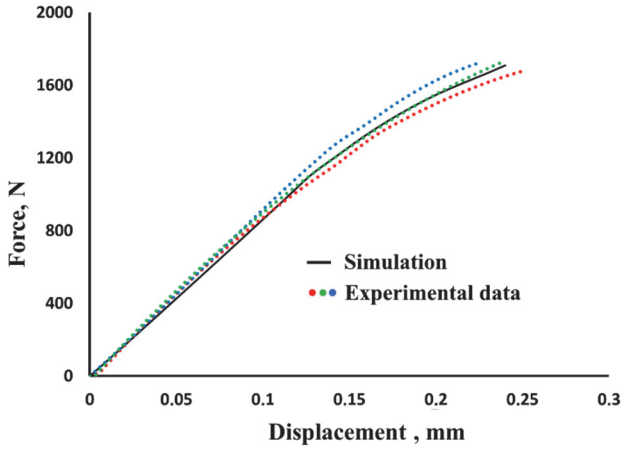

Figure 5: Comparison of the experimental and finite element simulation force-displacement curves for compression of cylindrical reinforced epoxy resin specimens at a test temperature of 25 °C.

The simulation resulted in the evaluation of the changes in the stress and strain tensor components, which are necessary to calculate the parameters k and μ_σ, ε_{eq} and σ_{eq} at each loading step.

As an example, fig. 6a shows a finite element model of cylindrical specimen compression and the cross-sectional distribution of ε_{eq} at fracture. Although the highest strain is localized in the central region of the specimen, the disruptive crack occurs in the middle of the lateral surface of the specimen, this being caused by the appearance of tensile tangential stresses with surface warping due to the inhibiting effect of the friction forces at the tool–specimen interface. Herewith, the parameters k and μ_σ change from their initial values $\mu_\sigma = 1$ and $k = -\frac{1}{\sqrt{3}}$ (fig. 6 b).

The above-discussed approach to constructing a finite-element model was used to study the stress-strain state in other types of testing, which are discussed in what follows.

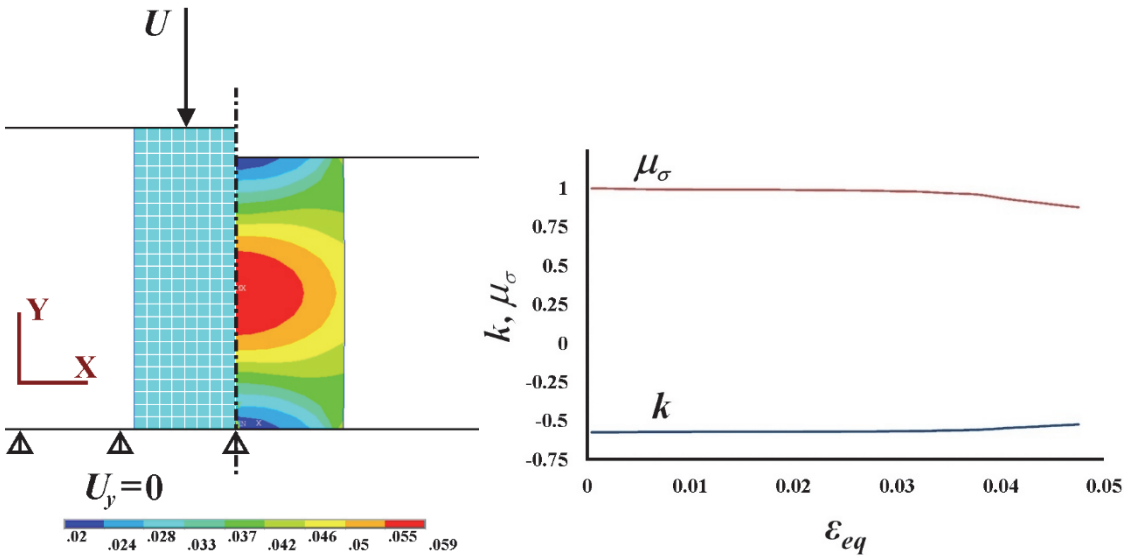

(a) (b)

Figure 6: Simulation results of compressing a cylindrical pure epoxy resin specimen at a test temperature of 25 °C: (a) initial finite element mesh (left); cross-sectional distribution of ε_{eq} at fracture (right); and (b) the behavior of the parameters k and μ_σ at the crack initiation site (the middle of the lateral surface of the specimen).

Tension of bell-shaped specimens

A punch was placed into the cylindrical hollow of the specimen (fig. 7 a), and this assembly was then put on a ring with an inner diameter slightly exceeding the diameter of the lower part of the specimen (fig. 7 a). The specimen was loaded by applying a compressive force to the punch. As a result, the material volume in the transition part between the upper and lower parts of the specimen experienced localized shear strain followed by fracture (fig. 7 b).

Fig. 8 shows the finite-element model of the testing process and the cross-sectional distribution of ε_{eq} at fracture. The number of finite elements in the model is 821. The element size is 0.2 mm.

The results of the visual examination of the specimens after testing (fig. 7 b) were compared with the simulation results (fig. 8). The comparison testifies that the specimens fracture at the site of maximum equivalent strain on the external surface of the transition zone. The moment of fracture was identified in the testing by a sharp decrease in the deformation force.

Fig. 9 shows the behavior of the stress triaxiality parameter k and the Lode–Nadai coefficient μ_σ at the site of failure in the testing of a bell-shaped pure epoxy resin specimen at 25 °C.

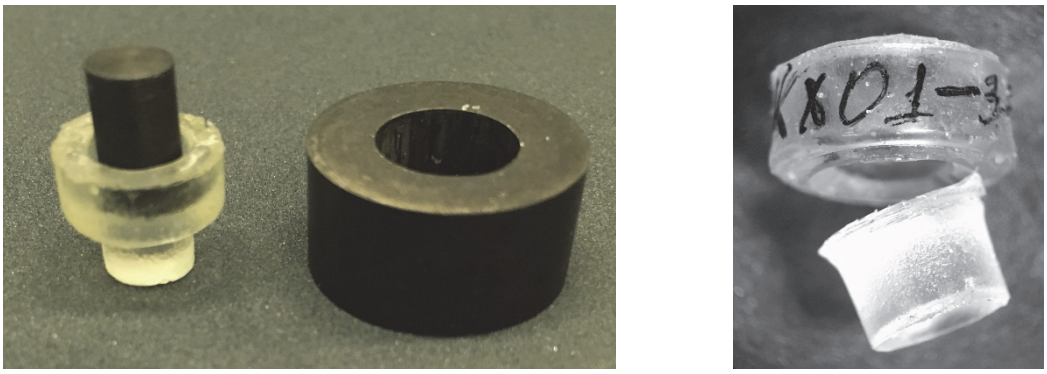

(a) (b)

Figure 7: The bell-shaped pure epoxy resin specimen under tensile testing: the equipped specimen before testing (a); the failed specimen (b).

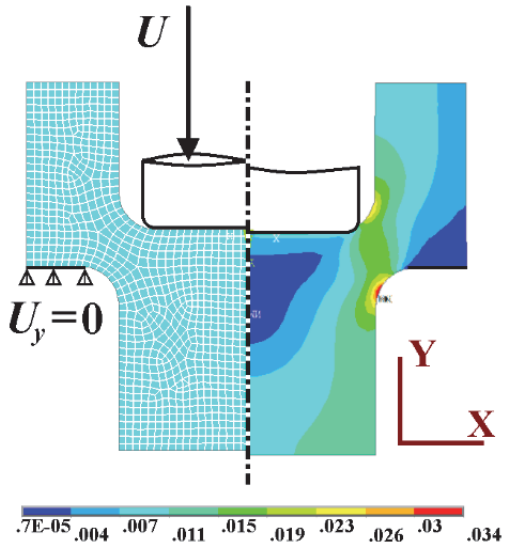

Figure 8: The finite-element mesh of the model of the bell-shaped tensile specimen (left); the cross-sectional distribution of equivalent strain ε_{eq} at failure (right).

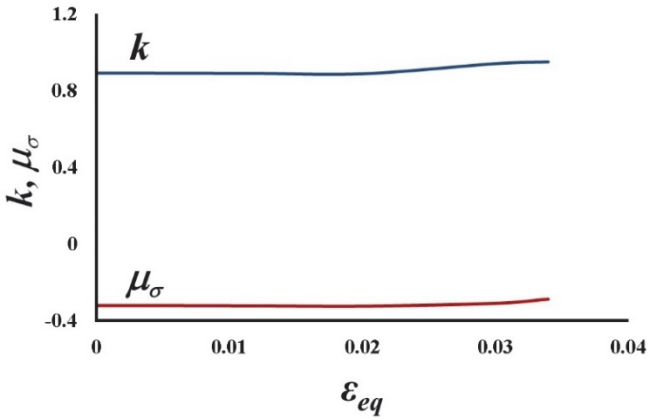

Figure 9: The behavior of the parameters k and μ_σ of the bell-shaped tensile specimen at the site of failure on the external surface of the transition zone.

Compression of bell-shaped specimens

The specimens were mounted onto an immobile flat die in the testing machine and subjected to a compressive force applied to the upper end face of the specimen (fig. 10 a). Fracture occurred near the internal surface of the specimen transition zone (fig. 10 b).

Fig. 11 shows the finite-element model of the testing process and the cross-sectional distribution of ε_{eq} at fracture. The number of finite elements in the model is 670. The element size is 0.2 mm. The simulation (fig. 11) shows that the highest strain is accumulated on the external surface of the transition zone, although fracture occurred in another zone of the specimen. This must be due to more favorable stress state implemented there ($k = -0.86$ in the initial stage of deformation, and this parameter subsequently decreases to $k < -1$), which prevents the appearance of a disruptive crack (fig. 12 a). On the internal surface of the transition zone the stress triaxiality parameter is twice as high at the beginning of deformation, $k = -0.42$ (fig. 12 b). The values of the Lode–Nadai parameter μ_σ become stabilized near 0 with developed plastic strain.

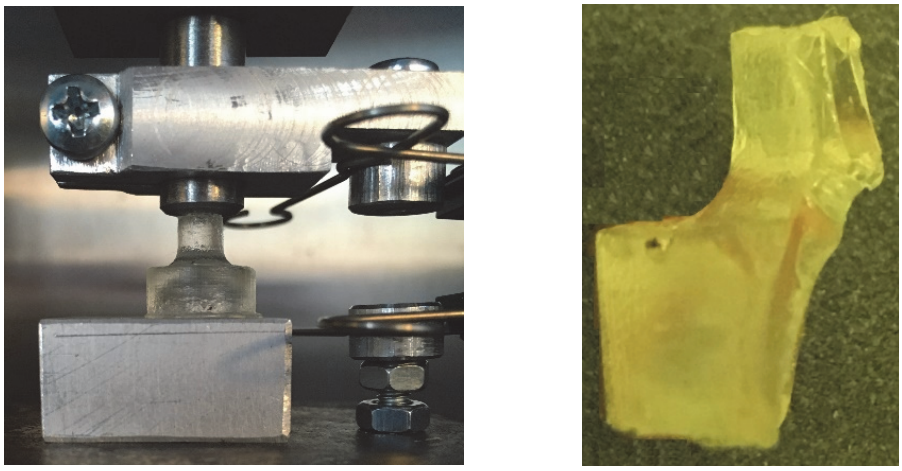

(a) (b)

Figure 10: The bell-shaped pure epoxy resin specimen under compressive testing before (a) and after (b) testing.

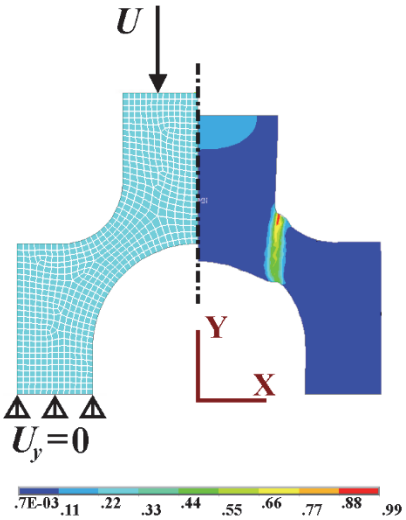

Figure 11: The finite-element model of bell-shaped specimen compression (left) and the cross-sectional distribution of strains ε_{eq} at fracture (right).

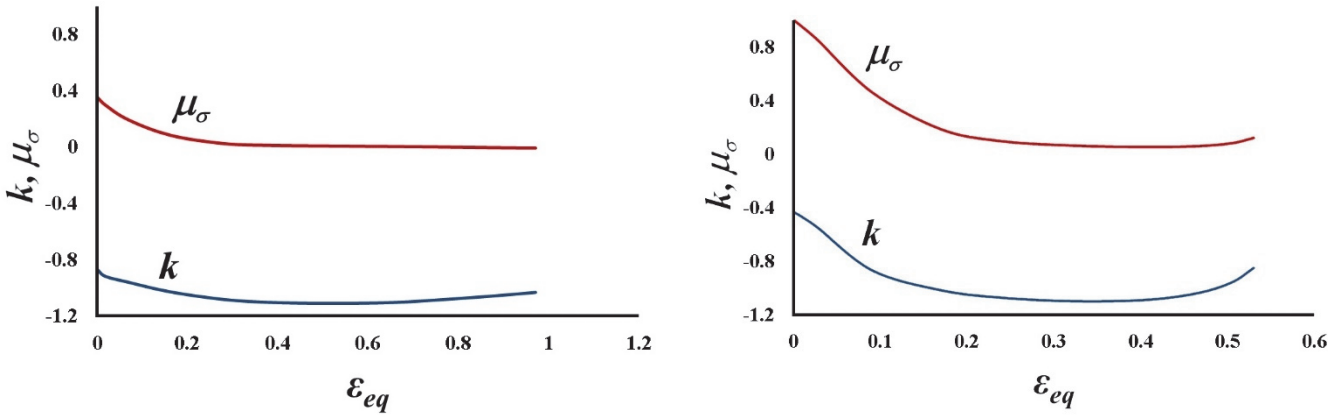

(a) (b)

Figure 12: The behavior of the stress parameters k and μ_σ of the bell-shaped specimen under compression (reinforced epoxy resin, 25 °C): on the external surface of the transition zone (a) and at the site of crack initiation on the internal surface (b).

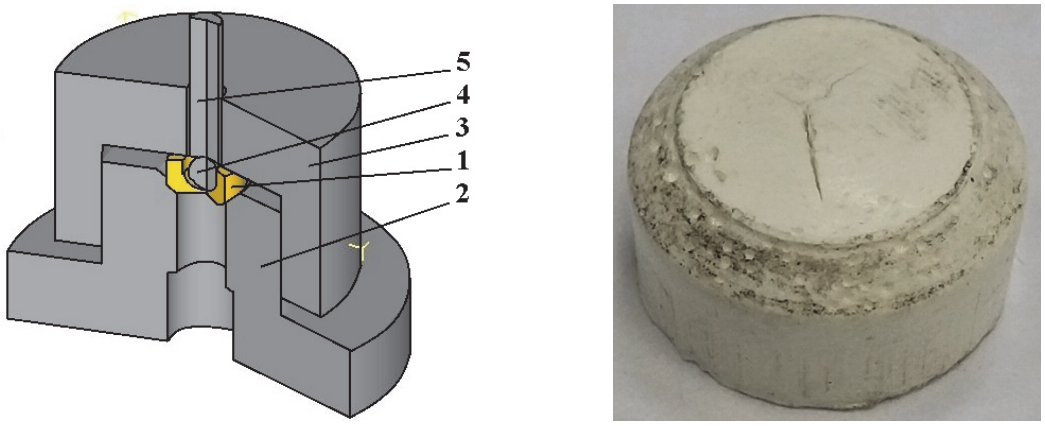

(a) (b)

Figure 13: A thick-walled cup-shaped specimen made of reinforced epoxy resin: specimen installation diagram (a) and the fractured specimen after testing (b).

Dishing of a thick-walled cup-shaped specimen

The test specimen 1 (fig. 13 a) was placed on the base 2 in the workspace of the testing machine and fixed by a cap 3 threaded to the base. A steel ball 4 was put inside the specimen and then a force from the testing machine was applied through a punch 5. The design of the specimen provided the appearance of the initial fracture zone in the center of the external surface of the bottom, as shown in the photograph (fig. 13 b).

Fig. 14 shows the finite element model of the testing process and the cross-sectional distribution of ε_{eq} at fracture. The number of finite elements in the model is 2734. The element size is 0.15 mm.

The analysis of the results of simulating the testing process shows that the most unfavorable stress-strain state is found near the middle of the external surface of the dished bottom (fig. 14). The highest value of accumulated strain ε_{eq} and intensive tensile stresses $(k=1.15)$ are responsible for the appearance of incipient failure here. The Lode–Nadai coefficient is the same as for upsetting of cylindrical specimens, $\mu_\sigma = 1$ (fig. 15).

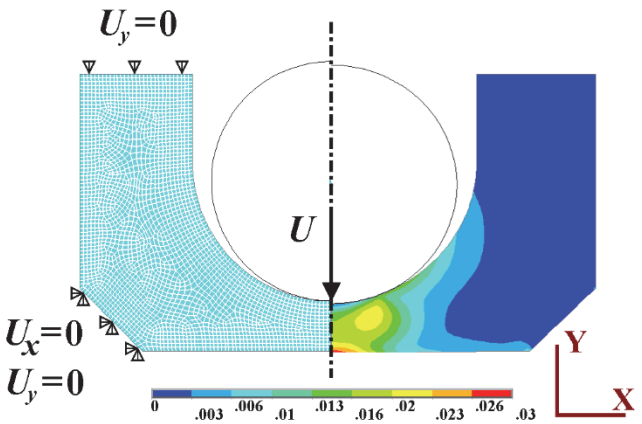

Figure 14: The finite-element model of dishing in a thick-walled cup-shaped specimen (left) and the cross-sectional distribution of the values of equivalent stain ε_{eq} at fracture (right).

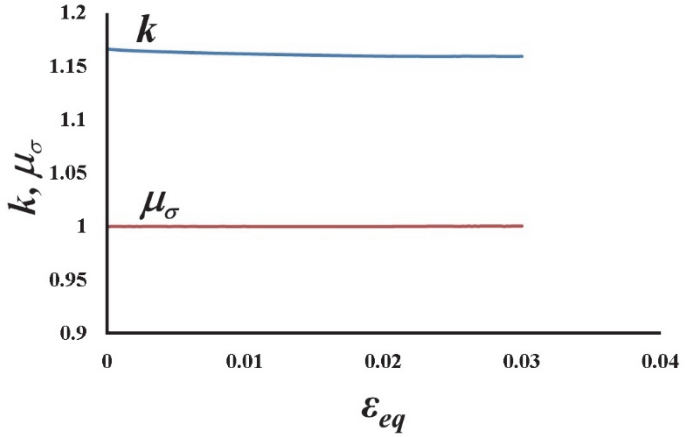

Figure 15: The behavior of the parameters in the middle of the external surface of the bottom in the thick-walled cup-shaped specimen, where a disruptive crack is initiated (pure epoxy resin, room temperature).

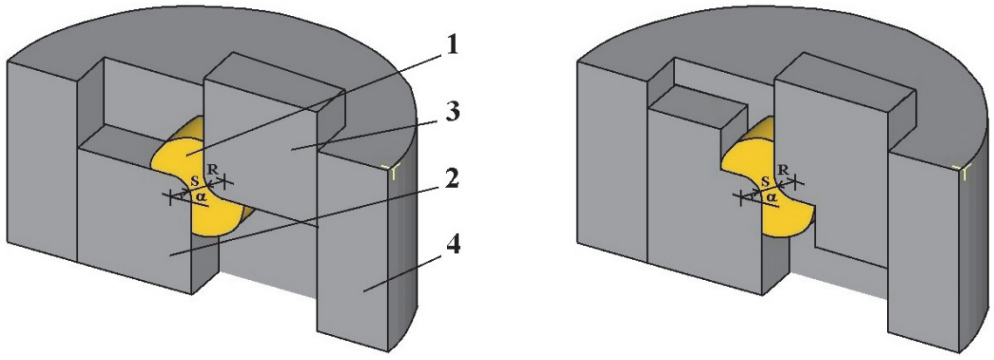

(a) (b)

Figure 16: The diagram of oblique dog-bone-shaped specimen testing: dies without a lateral support (a); dies with a lateral support (b).

Testing of oblique dog-bone-shaped specimens under plane shearing

The diagram of testing is shown in fig. 16. Before testing, the specimen was placed on a die 2 to be deformed by an upper die 3, through which a force is translated to the specimen. The horizontal displacement of the dies and the lateral surfaces of the specimen must be restricted. For this purpose, the specimen and the dies were placed in a container 4 (shown as a sectional view in fig. 16). More intricately shaped dies 2 and 3 can be used to apply additional compressive stresses (fig. 16 b), which restrict metal flow in the direction perpendicular to the motion of the upper die (the dies with a lateral support). During testing, the strain is localized in the central part of the specimen. The stress state in the deformation zone essentially depends on the ratio of the dimensions of the central part, namely central part thickness S, the spherical radius R, the

pitch α of the line connecting the spherical radii. Specimens of three dimension types were made for testing: 1) $R = 2$ mm, $S = 2$ mm, $\alpha = 30°$; 2) $R = 3$ mm, $S = 2.5$ mm, $\alpha = 50°$; 3) $R = 2$ mm, $S = 5$ mm, $\alpha = 80°$.

Figs. 17 a and 17 b show photographs of dimension type 1 specimens before and after testing as an example. Fig. 17 c shows the finite-element model used to analyze the stress-strain state in the course of testing. The front end face of the model corresponds to the symmetry plane at the half-width of the specimen. The finite element models of the specimens have the following characteristics.

Type I specimens: the number of finite elements is 5210 and the element size is 0.3 mm.

Type II specimens: the number of finite elements is 5160 and the element size is 0.3 mm.

Type III specimens: the number of finite elements is 6840 and the element size is 0.3 mm.

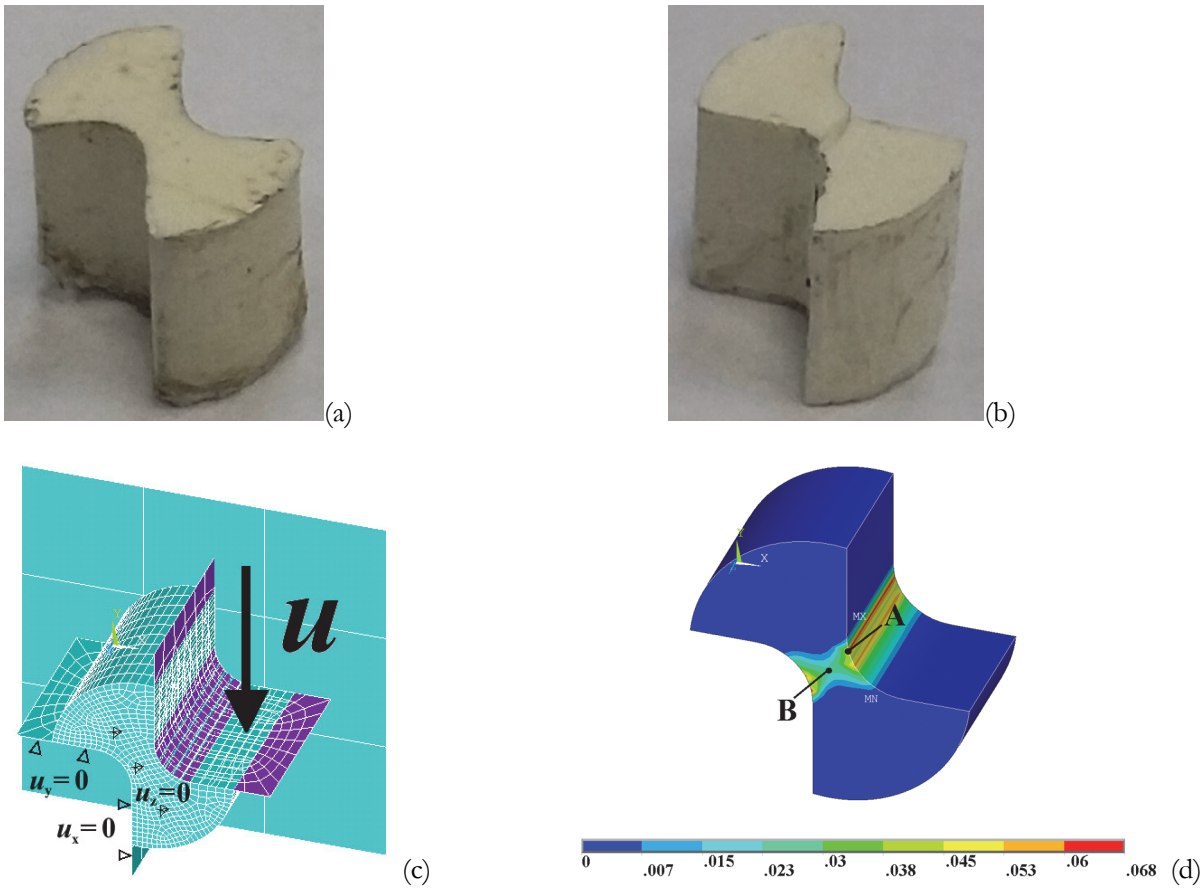

Figure 17: The oblique dog-bone-shaped specimen of dimension type 1: photographs of the specimen before (a) and after (b) testing; the 3D finite-element model (c); cross-sectional distribution of ε_{eq} at fracture (d) (reinforced epoxy resin, room temperature).

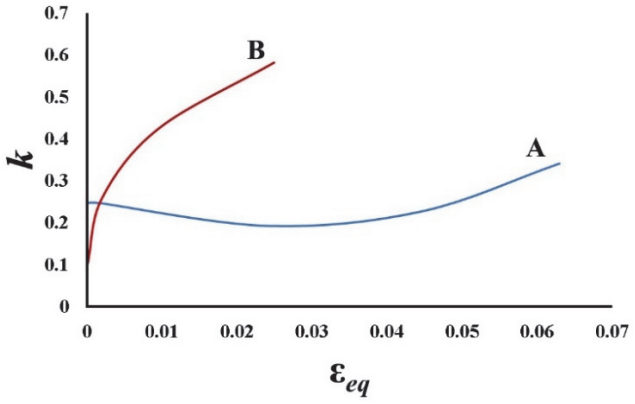

Figure 18: The behavior of k during the testing of the oblique dog-bone-shaped specimen of dimension type 1 (reinforced epoxy resin, room temperature).

The maximum strain is localized on the specimen–die interface at point A (fig. 17 d). However, most probably, fracture is initiated in the central part of the specimen (point B in fig. 17 d) since a more unfavorable stress state occurs here (fig. 18). The Lode–Nadai coefficient is close to zero at both points.

DIAGRAMS OF ULTIMATE STRAIN ENERGY DENSITY (FRACTURE LOCI)

Strain energy density W_f is used as the quantitative parameter characterizing the limiting state of epoxy resin in cohesive failure:

$$W_f = \int_0^{\varepsilon_{eq}^*} \sigma_{eq}\left(\varepsilon_{eq}\right) d\varepsilon_{eq} \tag{9}$$

where ε_{eq}^* is ultimate strain at the site of failure.

The value of W_f for each material depends on the stress state characterized by the totality of the parameters k and μ_σ, as well as temperature and strain rate. Rigorously, to construct the fracture locus, W_f must be determined in experiments conducted at constant values of k and μ_σ. However, it follows from the above dependences that the stress state is hardly invariable during testing; therefore, the quantitative dependence $W_f\left(k, \mu_\sigma\right)$ can be established only by using the averaged values of the stress parameters or by the identification procedure. The latter way is used in this study. Strain energy density W^* at the crack initiation site is evaluated from the simulation of the testing process with account taken of the stress-strain history.

The values of ε_{eq}^* and W^* reached at the site of failure and averaged from the simulation results are shown in Tab. 2.

Specimen, type of testing	T, °C	Reinforced epoxy resin		Pure epoxy resin	
		ε_{eq}^*	W^*, MJ/m³	ε_{eq}^*	W^*, MJ/m³
Cylindrical, compression	25	0.052	4.65	0.047	3.38
	-50	0.04	4.14	0.023	1.53
Bell-shaped, tension	25			0.033	1.31
	-50			0.034	3.23
Bell-shaped, compression	25			0.529	106.83
	-50			0.07	13.63
Thick-walled cup, dishing	25	0.037	2.74	0.029	1.44
	-50	0.022	1.34	0.024	1.63
Plane shear $R = 2$ mm, $S = 2$ mm, $\alpha = 30°$	25	0.025	4.41		
	-50	0.047	5.63		
Plane shear $R = 3$ mm, $S = 2.5$ mm, $\alpha = 50°$	25	0.078	8.07		
	-50	0.079	11.7		
Plane shear $R = 2$ mm, $S = 5$ mm, $\alpha = 80°$	25	0.18	21.13		
	-50				

Table 2: The data for identifying the dependence $W_f = f\left(k, \mu_\sigma\right)$.

As the objective function for the identification of the dependence $W_f = f\left(k, \mu_\sigma\right)$, the criterion for the failure of the linear model of material damage ω under deformation is used in the following interpretation:

$$\omega = \int_0^{\varepsilon_{eq}} \frac{dW}{W_f} = 1 \tag{10}$$

During deformation, damage ω varies from 0 before the deformation starts to 1 at the moment of crack initiation, and the intermediate values of ω characterize the amount of microscopic material damage by strain-induced defects. Assume that, at a fixed test temperature, the dependence $W_f = f(k, \mu_\sigma)$ can be described by the approximating linear function:

$$W_f = C_0(k) + C_1(k)\mu_\sigma \tag{11}$$

where $C_0(k)$ and $C_1(k)$ are the unknown functions of the stress triaxiality factor k. To describe the k dependence of W_f at fixed values of μ_σ, similarly to [7], the study uses the exponential law:

$$W_f = \alpha \exp(-\beta k) \tag{12}$$

where α and β are empirical coefficients.

Let α_0, α_{+1}, β_0 and β_{+1} have the values of the coefficients α and β when $\mu_\sigma = 0$ and $\mu_\sigma = 1$, respectively, then it follows from Eqn. (12) that:

$$W_f(k, 0) = \alpha_0 \exp(-\beta_0 k) \tag{13}$$

$$W_f(k, +1) = \alpha_{+1} \exp(-\beta_{+1} k) \tag{14}$$

Substituting the right-hand sides of Eqs. (13) and (14) and the corresponding values of μ_σ into Eqn. (11), after some transformations we find expressions for $C_0(k)$ and $C_1(k)$ and obtain the interpolation formula:

$$W_f(k, \mu_\sigma) = \alpha_0 \exp(-\beta_0 k)(1 - \mu_\sigma) + \alpha_{+1} \exp(-\beta_{+1} k)\mu_\sigma \tag{15}$$

For the parametric identification of Eqn. (15), we use the data from Tab. 2 and the dependences $k(\varepsilon_{eq})$ and $\mu_\sigma(\varepsilon_{eq})$ during the testing, which are partially shown in figs. 6, 9, 12, 15, and 18. The functional of squared deviations (16) of the objective function (10) from 1 is minimized by varying the coefficients α_0, α_{+1}, β_0 and β_{+1}.

$$\sum_{i=1}^{n} (1 - \omega_i)^2 \to \min \tag{16}$$

where n is the number of types of testing at the given temperature.

The coefficients are varied by the Hooke–Jeeves method [25]. As a result of searching, it is possible to hit the local minimum of the functional (16); therefore, we select not one initial search point, but a certain set of points. The Hooke–Jeeves procedure is performed for each initial search point. The found values of the coefficients are presented in Tab. 3. When calculating by Eqn. (10), as the upper limit of integration, we substitute the values of ε_{eq} from Tab. 2, which were reached at the site of failure during the tests. The identification error is less than 12%.

Material	T, °C	Coefficients in Eqn. (15)			
		α_0, MJ/m³	β_0	α_{+1}, MJ/m³	β_{+1}
Reinforced epoxy resin	25	7.52	1.87	3.92	0.3
	-50	10.79	3.23	2.85	0.65
Pure epoxy resin	25	10.47	2.24	2.11	0.31
	-50	7.47	1.09	1.48	0.021

Table 3: Identification results.

The fracture loci constructed from the data presented in Tab. 3 are shown in fig. 19 as 3D diagrams of ultimate strain energy density. To make a comparative analysis of the effect of the factors, we consider the characteristic sections of the fracture loci corresponding to the plane strain state $(\mu_\sigma = 0)$ and axisymmetric compression $(\mu_\sigma = 1)$. Fig. 20 shows sections of the fracture locus obtained from the results of testing at room temperature, and Fig. 21 shows sections of the diagram based on the results of testing at −50 °C.

The reported data suggest that W_f predictably tends to increase with the share of compressive stresses (with decreasing k), although this effect for deformation at −50 °C is practically unnoticeable under axisymmetric compression (fig. 21 b). In the general case, the effect of the test temperature and the stress parameters manifests itself ambiguously in the values of ultimate strain energy density for the studied materials. Thus, for shear $(\mu_\sigma = 0)$ at 25 °C, the value of W_f is higher for epoxy resin in the entire range of k (fig. 20 a), though at −50 °C W_f is higher for reinforced epoxy resin in the range of compressive stresses $(k < 0)$, but lower under tensile stresses (fig. 21 a). Under axisymmetric compressive strain $(\mu_\sigma = 1)$, W_f is higher for reinforced epoxy resin at both test temperatures and in the entire range of k.

The obtained dependences can be used to make design and checking calculations of structural components and their adhesive joints.

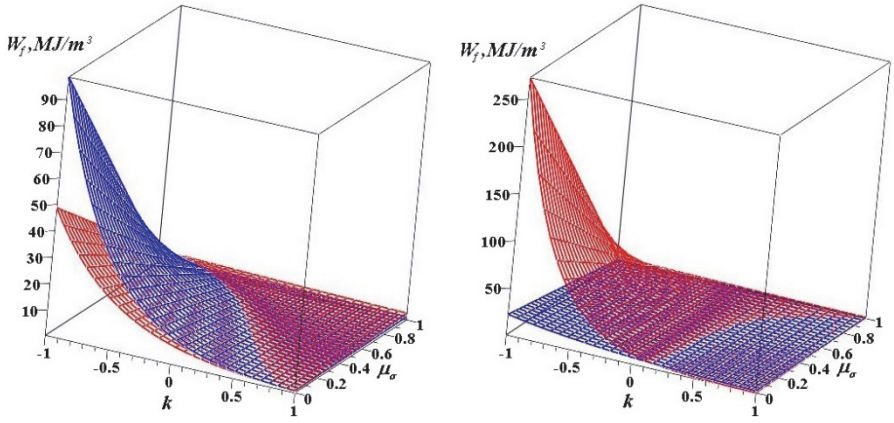

(a) (b)

Figure 19: Fracture loci for pure epoxy resin (blue) and reinforced epoxy resin (red) at test temperatures of 25 °C (a) and −50 °C (b).

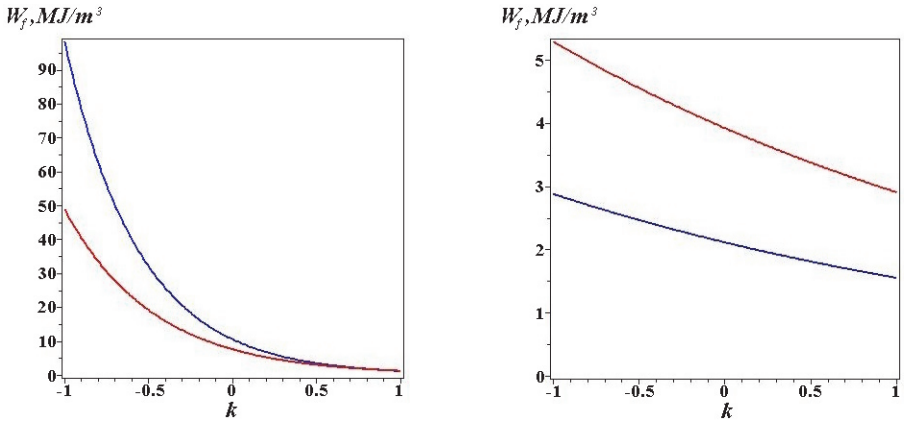

(a) (b)

Figure 20: Sections of the fracture loci for pure epoxy resin (blue) and reinforced epoxy resin (red) at test temperatures of 25 °C with $\mu_\sigma = 0$ (a) and $\mu_\sigma = 1$ (b).

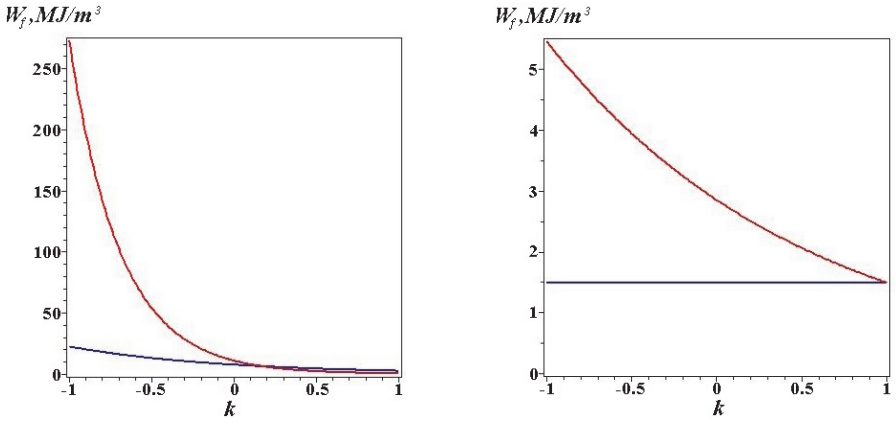

(a) (b)

Figure 21: Sections of the fracture loci for pure epoxy resin (blue) and reinforced epoxy resin (red) at test temperatures of -50 °C with $\mu_\sigma = 0$ (a) and $\mu_\sigma = 1$ (b).

CONCLUSION

The study has demonstrated the possibility of constructing a fracture locus for engineering organic polymer materials as a dependence of ultimate strain energy density in cohesive failure on the stress triaxiality factor in the range $-1 \le k \le 1$ and the Lode–Nadai coefficient in the range $0 \le \mu_\sigma \le 1$, based on an original set of testing. The obtained fracture loci make it possible to assess failure under multiaxial loading under conditions of tensile and compressive stresses. To construct the fracture loci, epoxy resin reinforced with 10% of TiO_2 and pure epoxy resin were used to make specially shaped specimens, namely bell-shaped specimens for shearing under tension and compression, thick-walled cups for dishing, cylindrical specimens for compression, and oblique dog-bone-shaped specimens. The specimens were loaded to failure at 25 and 50 °C. To determine the behavior of k and μ_σ, finite-element simulation of the testing process was made in Ansys. The parametric identification of the fracture locus was made with the use of experiment and simulation results.

The analysis of the research results allows the following conclusions to be drawn:

1. Introduction of 10% of TiO_2 nanoparticles increases the strength properties of epoxy resin; namely, the normal elastic modulus increases by 14 and 11% at $T = -50$ and 25 °C, respectively, and ultimate compressive strength increases by 25 and 35% at $T = -50$ and 25 °C, respectively.
2. In the general case, the effect of test temperature and the stress parameters manifests itself ambiguously in the values of ultimate strain energy density W_f for the studied materials. Thus, for shear $(\mu_\sigma = 0)$ at 25 °C, the value of W_f is higher for epoxy resin in the entire range of k, though at −50 °C W_f is higher for reinforced epoxy resin in the range of compressive stresses $(k < 0)$, but lower under tensile stresses. Under axisymmetric compressive strain, the value of W_f is higher for reinforced epoxy resin at both test temperatures and in the entire range of k.
3. The obtained fracture loci can be used to make design and checking calculations of structural components and their adhesive joints.

ACKNOWLEDGEMENTS

The study was financially supported by the Russian Science Foundation, grant No. 24-29-00528. The specimens were made at the SAOS shared research facilities center, IOS UB RAS. The equipment of the Plastometriya shared research facilities, IES UB RAS, was used to perform the tests.

Finite element simulation of the stress-strain state during testing was performed in the Ansys software by the URAN supercomputer at the shared research facilities center of the IMM UB RAS.

REFERENCES

[1] Barbero, E.J., Shahbazi, M. (2017). Determination of material properties for ANSYS progressive damage analysis of laminated composites, Compos. Struct., 176, pp. 768–779. DOI: https://doi.org/10.1016/j.compstruct.2017.05.074.

[2] Tserpes, K., Barroso-Caro, A., Carraro, P.A., Beber, V.C., Floros, I., Gamon, W., Kozłowski, M., Santandrea, F., Shahverdi, M., Skejić, D., Bedon, C., Rajčić, V. (2022). A review on failure theories and simulation models for adhesive joints, Journal of Adhesion, pp. 1855–1915. DOI: https://doi.org/10.1080/00218464.2021.1941903.

[3] Kolmogorov, V.L., Shishmintsev, L.F. (1966). Ductility of steel as a function of hydrostatic pressure, Phys. Met. Metallogr., 21(6), pp. 97–101.

[4] Nouira, M., Cristina Oliveira, M., Khalfallah, A., Luís Alves, J. and Filipe Menezes, L. (2023). Comparative fracture prediction study for two materials under a wide range of stress states using seven uncoupled models. Engineering Fracture Mechanics, 279. https://doi.org/10.1016/j.engfracmech.2022.108952

[5] Fincato, R., Tsutsumi, S. (2022). Ductile fracture modeling of metallic materials: A short review, Frattura Ed Integrita Strutturale, 16(59), pp. 1–17. DOI: https://doi.org/10.3221/IGF-ESIS.59.01.

[6] Alam, M. F., Balaji, V., Tucci, F., Krishnaswamy, H. and Chakkingal, U. (2025). A critical evaluation of shear specimen geometry for accurate stress triaxiality control. Engineering Fracture Mechanics, 328. DOI: https://doi.org/10.1016/j.engfracmech.2025.111562

[7] Smirnov, S. V., Vichuzhanin, D.I., Nesterenko, A. V. (2015). A set of tests for studying the effect of the stress state on ultimate metal plasticity at high temperature, PNRPU Mechanics Bulletin, 2015(3), pp. 146–164. DOI: https://doi.org/10.15593/perm.mech/2015.3.11.

[8] Zhao, W., Zhao, C., Zhang, G., Wang, T. and Huang, Q. (2025). Damage evolution under negative stress triaxiality: Experiments and modeling. International Journal of Mechanical Sciences, 305. DOI: https://doi.org/10.1016/j.ijmecsci.2025.110777

[9] Zhou, J. and Gardner, L. (2025). New void growth-based ductile fracture models incorporating interaction effects of stress triaxiality and Lode angle parameter. Theoretical and Applied Fracture Mechanics, 140. DOI: https://doi.org/10.1016/j.tafmec.2025.105204

[10] Han, L.M., Xue, S.F., Zhang, Y. (2020). Effect of stress triaxiality on the damage of polyethylene., IOP Conference Series: Materials Science and Engineering, vol. vol. 770, Institute of Physics Publishing. DOI: https://doi.org/10.1088/1757-899X/770/1/012072.

[11] Saada, K., Amroune, S., Zaoui, M. (2023). Prediction of mechanical behavior of epoxy polymer using Artificial Neural Networks (ANN) and Response Surface Methodology (RSM), Frattura Ed Integrita Strutturale, 17(66), pp. 191–206. DOI: https://doi.org/10.3221/IGF-ESIS.66.12.

[12] Altenbach, P.H., Tushtev, K. (2001). A new static failure criterion for isotropic polymers, Mech. Compos. Mater., 37(5/6), pp. 475–482. DOI: https://doi.org/10.1023/A:1014269314272.

[13] Morelle, X.P., Chevalier, J., Bailly, C., Pardoen, T., Lani, F. (2017). Mechanical characterization and modeling of the deformation and failure of the highly crosslinked RTM6 epoxy resin, Mech. Time Depend. Mater., 21(3), pp. 419–454. DOI: https://doi.org/10.1007/s11043-016-9336-6.

[14] Hu, Y., Xia, Z., Ellyin, F. (2003). Deformation behavior of an epoxy resin subject to multiaxial loadings. Part I: experimental investigations, Polym. Eng. Sci., 43(3), pp. 721–733. DOI: https://doi.org/10.1002/pen.10060.

[15] Bridgman, P.W. (1964) Studies in large plastic flow and fracture: with special emphasis on the effects of hydrostatic pressure, Cambridge, Harvard University Press.

[16] Wu, P. D., Embury, J. D., Lloyd, D. J., Huang, Y., Neale, K. W. (2009) Effects of superimposed hydrostatic pressure on sheet metal formability, Int. J. Plast., 25(9), pp. 1711–1725. DOI: https://doi.org/10.1016/j.ijplas.2008.10.002.

[17] Malcher, L., Mamiya, E.N. (2014). An improved damage evolution law based on continuum damage mechanics and its dependence on both stress triaxiality and the third invariant, Int. J. Plast., 56, pp. 232–261. DOI: https://doi.org/10.1016/j.ijplas.2014.01.002.

[18] Morin, L., Leblond, J.B., Mohr, D., Kondo, D. (2017). Prediction of shear-dominated ductile fracture in a butterfly specimen using a model of plastic porous solids including void shape effects, European Journal of Mechanics, A/Solids, 61, pp. 433–442. DOI: https://doi.org/10.1016/j.euromechsol.2016.10.014.

[19] Tang, B., Wu, F., Wang, Q., Liu, J., Guo, N., Ge, H., Wang, Q., Liu, P. (2020). Damage prediction of hot stamped boron steel 22MnB5 with a microscopic motivated ductile fracture criterion: Experiment and simulation, Int. J. Mech. Sci., 169. DOI: https://doi.org/10.1016/j.ijmecsci.2019.105302.

[20] Smirnov, S., Vichuzhanin, D., Nesterenko, A., Smirnov, A., Pugacheva, N., Konovalov, A. (2017). A fracture locus for a 50 volume-percent Al/SiC metal matrix composite at high temperature, International Journal of Material Forming, 10(5), pp. 831–843. DOI: https://doi.org/10.1007/s12289-016-1323-6.

[21] Vichuzhanin, D.I., Yolshina, L.A., Muradymov, R. V., Nesterenko, A. V. (2018). A fracture locus for a 1 wt% aluminum-graphene metal matrix composite at 300°C, Letters on Materials, 8(2), pp. 184–189. DOI: https://doi.org/10.22226/2410-3535-2018-2-184-189.

[22] Vichuzhanin, D.I., Shevchenko, V.G., Eselevich, D.A. (2025) Fracture locus of a selective laser melted Al–2.3% V alloy, Russ. Metall. (Metally), 4, pp. 8–18. DOI: https://doi.org/10.1134/S0036029525700028.

[23] Smirnov, S. V., Veretennikova, I. A., Pestov, A. V., Konovalov, D. A., Smirnova, E. O. and Osipova, V. A. (2023). Effect of the Nature of Oxide Nanofillers on Changes in the Mechanical Properties of Epoxy Coatings under Thermal Cycling, Mechanics of Advanced Composite Structures, 10(1), pp. 195–204. DOI: https://doi.org/10.22075/macs.2022.26989.1399.

[24] Shetty, S., Nilsson, L. (2017). An evaluation of simple techniques to model the variation in strain hardening behavior of steel, Struct. Multidisc. Optim., 55(3), pp. 945–957. DOI: https://doi.org/10.1007/s00158-016-1547-6.

[25] Hooke, R., Jeeves, T.A. (1961) Direct Search. Solution of Numerical and Statistical Problems, Journal of the ACM, 8, pp. 212–229. DOI: https://doi.org/10.1145/321069.